Electron energy-loss near-edge shape as a probe to investigate the stabilization of yttria-stabilized zirconia

S. Ostanin,[1,2,*] A. J. Craven,[1] D. W. McComb,[2] D. Vlachos,[1,2,†] A. Alavi,[3] A. T. Paxton,[4] and M. W. Finnis[4]

[1]*Department of Physics and Astronomy, University of Glasgow, Glasgow G12 8QQ, United Kingdom*

[2]*Department of Chemistry, University of Glasgow, Glasgow G12 8QQ, United Kingdom*

[3]*Department of Chemistry, University of Cambridge, Cambridge CB2 1EW, United Kingdom*

[4]*Atomistic Simulation Group, School of Mathematics and Physics, Queen's University, Belfast BT7 1NN, United Kingdom*

The electron energy-loss near-edge structure (ELNES) at the O K edge has been studied in yttria-stabilized zirconia (YSZ). The electronic structure of YSZ for compositions between 3 and 15 mol % Y_2O_3 has been computed using a pseudopotential-based technique to calculate the local relaxations near the O vacancies. The results showed phase transition from the tetragonal to cubic YSZ at 10 mol % of Y_2O_3, reproducing experimental observations. Using the relaxed defect geometry, calculation of the ELNES was carried out using the full-potential linear muffin-tin orbital method. The results show very good agreement with the experimental O K-edge signal, demonstrating the power of using ELNES to probe the stabilization mechanism in doped metal oxides.

I. INTRODUCTION

Investigation of concentration-temperature phase diagrams can significantly improve the understanding of the factors controlling material properties. Yttria-stabilized zirconia (YSZ), formed by the addition of Y_2O_3 to ZrO_2, is one such material with numerous commercial applications.[1] Pure ZrO_2 exhibits three well-defined polymorphs: the low-temperature monoclinic (m) phase, the tetragonal (t) phase between 1170 and 2370 °C, and the high-temperature cubic (c) phase, which exists up to the melting point of 2680 °C. Y_2O_3 has a large solid solubility range in ZrO_2 and hence can be used to stabilize the t phase of YSZ, $(Y_2O_3)_x(ZrO_2)_{1-x}$, over the composition range $0.02 < x < 0.09$ and the c phase with $0.04 < x < 0.4$.

Pure c-ZrO_2 has the fluorite structure with each metal ion in regular eightfold-coordinated sites having all of the Zr-O bonds of equal length. In the t phase, the Zr^{4+} ions are located in distorted eightfold coordination environments while, in m-ZrO_2, Zr^{4+} is found in sevenfold coordination. In YSZ, the trivalent dopant cations Y^{3+} substitute for some of the Zr^{4+} ions and, in order to maintain charge neutrality assuming formal ionic charges, one O vacancy ($\square$) must be created for each pair of dopant cations. The presence of $\square$'s reduces the average cation coordination number to a value between 7 and 8 depending on the dopant concentration. Thus, c- and t-YSZ contain relaxed defects such as the $\square$'s and Y-substituted atoms. These defects make the local atomic environments of the stabilized crystals rather different from the corresponding stoichiometric phases. The O $\square$'s may have a considerable influence on the mechanism of disordering and therefore on the YSZ phase diagram.

To date, no full quantitative description of the stabilization mechanism of YSZ has been reported. Extended x-ray absorption fine structure (EXAFS) results, which allow the individual coordination polyhedra to be probed, are somewhat contradictory. Some investigations have suggested that a Y ion is nearest-neighbor (NN) to the vacancy[2] while other investigations have suggested that Y occupies next-nearest neighbor (NNN) cation sites.[3] These inconsistencies are partly due to experiments being performed on samples with different dopant concentrations, leading to different displacements of the regular fluorite lattice sites near to the O $\square$. Recent x-ray and neutron diffraction experiments report that at low ($x < 0.15$) concentrations of Y_2O_3 there are regions ~ 15–20 Å in size which contain (i) isolated O $\square$ and (ii) $\square$'s arranged in pairs on the NN anion sites in the [111] fluorite direction, with the cation site located between them occupied by a Zr^{4+} ion.[4] The isolated $\square$'s, whose number increases with x, cause the t distortions observed clearly at $x < 0.09$. Goff and co-workers[4] suggested that another type of defect cluster formed as the x increases: the $\square$ pairs along [111] pack together as in the $Zr_3Y_4O_{12}$ structural motif.[5] However, modeling such ordered structures is outside the scope of this paper.

Electron energy-loss spectroscopy (EELS) has developed into a powerful technique for investigation of the electronic states of crystals, providing information about the unoccupied density of states (DOS) via the energy-loss near-edge structure (ELNES). The ELNES data are both the site and symmetry projected due to the localized nature of the core-level excitation process and, hence, can be compared directly with the results of density functional theory calculations. ELNES is closely related to the x-ray absorption near-edge structure (XANES) but has the advantage that the local composition can be determined in inhomogeneous materials. The ELNES spectra of YSZ have been measured,[6] demonstrating the features of the experimental O K-edge shapes which depend on the crystal structures and the Y_2O_3 composition.[7] The calculated and observed O K-edge shapes in pure m-ZrO_2 agree well. However, there is gradually worsening agreement from the t to the c phase between the calculated shapes of the pure t- and c-ZrO_2 structures and the experimental O K-edge ELNES from 3 and 10 mol % Y_2O_3-ZrO_2,

respectively. This is attributed to the absence of defects in pure materials. Using a $Zr_2Y_2O_7$ cell,[7] which crudely models 33 mol % Y_2O_3, a satisfactory qualitative result for the O K-edge shape was obtained, indicating that the presence of relaxed defects is essential in the ELNES calculations. These ELNES findings suggested that it would be worthwhile to carry out calculations using larger unit cells to model YSZ.

II. EXPERIMENT

The YSZ samples were initially characterized using powder x-ray diffraction (XRD) to check phase purity and by analytical transmission electron microscopy to measure the grain size, Y/Zr composition ratio, and homogeneity. The Y/Zr ratio was determined by energy dispersive x-ray (EDX) spectroscopy. The ELNES investigations were carried out using a 100-kV VG HB5 dedicated scanning transmission electron microscope (STEM) with post-specimen lenses and equipped with a GATAN 666 parallel electron energy-loss spectrometry (PEELS) system. A convergence semiangle of 11 mrad was used, giving a probe diameter of ~ 1 nm and a probe current of ~ 0.2 nA. The collection semiangle used was 12.5 mrad. A background of the form AE^{-r} was removed from the O K-edge spectra, the low loss spectrum was used to deconvolute the plural scattering, and the spectra were then sharpened by deconvoluting the detector point spread function.[8] The PEELS spectra from a number grains of material were checked for consistency and then summed. This consistency check ensures that the data used have not been influenced by electron beam damage of the specimen. The summation over a number of different grains means that the data are averaged over a range of orientations. At each point from which PEELS data were recorded, EDX data were also recorded to give the local Y/Zr ratio.

III. MODEL

The approach presented consists firstly of a relaxation of the $(96-y)$-atom YSZ supercell in the presence of y vacancies followed by the calculation of the ELNES using the relaxed atom positions. This $(96-y)$-atom supercell has a lattice parameter of $2a$, where a is the lattice parameter of the conventional 12-atom fluorite cell. To relax the cells, we have used the plane-wave, pseudopotential-based free energy molecular dymanics (FEMD) technique.[9] As we have demonstrated,[7] the FEMD and near full-potential linear muffin-tin orbital (NFP-LMTO) methods[10] are in almost perfect agreement, reproducing the relative energetics of the three ZrO_2 phases at 0 K. The structure generated by FEMD is in equilibrium with respect to the LMTO forces. The total and site- and Mulliken-projected DOS of YSZ after relaxation are derived from the energy bands within NFP-LMTO method. With this large cell, it was not possible to calculate the matrix element for each site or include the effects of a core hole because of the much increased computing time required. However, for this system, the Mulliken-projected DOS can be used to give a reasonable approximation of the ELNES.[11] The excited atoms contributing to a particular ionization edge have a range of environments after relaxation.

Hence, the ELNES shape from each site must be aligned to take account of the binding energy appropriate to that site and then summed. In order to allow a direct comparison of the calculated ELNES shape with experiment, a broadening mechanism has been applied to take into account the initial- and final-state lifetime broadening. The Lorentzian linewidth for the final states has the E^2 form.[7,12] The initial-state lifetime broadening is a Lorentzian with the linewidth taken from atomic data.[13] Finally the theoretical ELNES spectra are convoluted with a Gaussian whose full width at half maximum matches the instrumental resolution.

IV. RESULTS AND DISCUSSION

A. Isolated vacancy

An isolated vacancy in YSZ has been studied using the 95-atom cubic supercell. The initial fractional coordinates of the metal atoms are those in the fluorite cell and two Y atoms are substituted for two Zr atoms. The initial fractional positions of the O atoms are either those in the cubic fluorite structure or those corresponding to the tetragonal distortion of the O atoms in the t structure. A single atom from the O sublattice is removed. This corresponds to 3.2 mol % Y_2O_3-ZrO_2. Fixing the unit cell volume at that of the theoretical equilibrium volume of c-ZrO_2—namely, 131 Å^3—we make the static FEMD optimization, allowing the internal coordinates of all atoms to be relaxed. The 3 mol % Y_2O_3-ZrO_2 specimens characterized using powder XRD indicate the t-type distortions of the O columns and, in addition, a c/a ratio of ~ 1.03 for the metal sublattice. The tetragonal distortion of the metal sublattice has little effect on the relaxation process, as has been shown for pure ZrO_2,[14] while requiring a significant increase in computation time. Thus we start with the t-distorted O sublattice, as in t-ZrO_2, but assume $c/a=1$ for metal sublattice. The total energy after relaxation is compared to that starting from the c geometry of O with the same Zr/Y configurations.

Figure 1 shows the c arrangement of atoms around the vacant O site before structural relaxation. Figure 1, in the upper diagram, shows a fluorite unit cell of side of length a with an oxygen anion at the origin. It has been divided into eight octants. The four sevenfold-coordinated NN cations to the $\square$ occupy the centers of alternate octants to create a tetrahedral arrangement around the vacant anion site. The NN anions to the $\square$ are located at the face centers of the fluorite unit cell while the second nearest anions (NNN) are positioned at the middle of each edge of the unit cell and the third nearest (NNNN) anions are at the corners of the unit cell. In order to illustrate the cation geometry it is useful to redraw figure as shown in the lower diagram of Fig. 1. In this diagram, the octants have metal cations rather than oxygen anions at the corners and the O vacancy is at the body center of the central cube. The six NN anions to the $\square$ are located at the body centers of the other octants in an octahedral arrangement. The four NN cations occupy half of the corners of the central cube, forming a tetrahedral arrangement around the vacancy. The 12 NNN cations occupy half of the 24 outer corners of the octants.
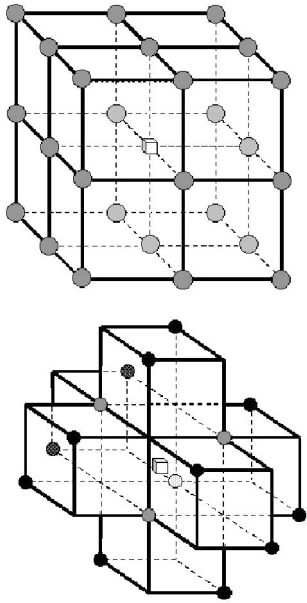
FIG. 1. Unrelaxed arrangement of atoms in pure c-ZrO2 in the vicinity of the vacant O site. In the upper diagram, the vacancy is at the center of the unit cell. The oxygen anions around the vacancy occupy the corners of the eight octants. In the lower diagram only the Zr cations are shown. The octants are the same size as in the upper diagram but the vacancy is at the center (rather than a corner) of an octant. The NN cations (gray) form a tetrahedral arrangement around the □ while the NNN cations (black) occupy 12 of the 24 corners of the outer octants.

With the O atoms in the c geometry, Stapper and co-workers[15] have reported that the NNN rather than the NN sites are favored for Y. Figure 2 shows the total energies of a range of relaxed and unrelaxed structures as a function of the nearest-neighbor shells in which the two Y atoms are placed. As will be seen below, the positions of Y atoms within a given shell have considerably less influence on the total energy. Panel (a) of Fig. 2 shows the unrelaxed structure with the O atoms in the c geometry. The configuration with the Y atoms adjacent to the □ [(NN,NN)] has the lowest energy. Panel (b) shows that relaxation reduces the total energy of all configurations by over 2 eV per 95-atom cell. It also shows that the configuration with both Y atoms in the NNN shell now has the lowest energy, as reported by Stapper and co-workers.[15]

Panel (c) shows the effect of starting relaxation with the O atoms in the t geometry. The total energies are reduced relative to the relaxed c configurations by ~ 1 eV/cell and the (NNN,NNN) Y pair remains the lowest-energy configuration. Experimentally, 3 mol % Y_2O_3-ZrO_2 can exist indefinitely in the t form. However, we have not calculated the m structure with 3 mol % Y_2O_3 and so cannot say whether the t structure is the stable form or only a metastable form.

These findings can be considered as a strong argument to support the evidence of Goff *et al.*[4] that, at low Y_2O_3 concentrations, the NN metal sites are occupied by Zr rather than Y. Placing Y in the NNN positions allows the coordination of Zr atoms in the NN sites to the □ to fall from 8 to 7. This is similar to the arrangement in the m phase. Y remains

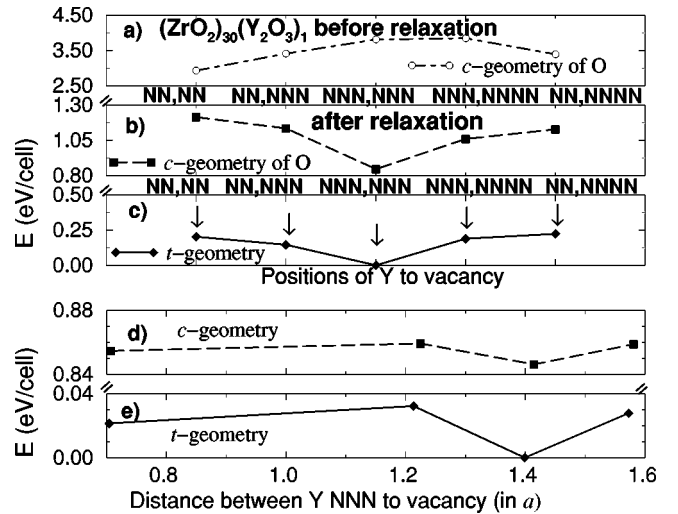

FIG. 2. Unrelaxed and relaxed energies of the single-vacancy c- and t-YSZ structures are plotted vs positions of the two Y dopant cations in the three upper panels, (a), (b), and (c). NN is the nearest-neighbor cation shell to the □ and so on. (NN,NNN) denotes the NN and NNN Y pair. The lower panels (d) and (e) present relaxation with Y NNN as a function of the Y-Y distance that illustrate a strong competition between all configurations.

eightfold coordinated. If the vacancies associate with host Zr ions, it may support a coordination-driven ordering model of stabilization in YSZ, which argues that increasing covalency can lower the coordination of Zr. This result is in conflict with a simple electrostatic model in which the repulsion between an anion vacancy and Y^{3+} should be less than between the □ and Zr^{4+}. However, it can be seen that the electrostatic-driven model works only when relaxation is forbidden.

Figure 1 shows there are 12 NNN cation sites on which the 10 Zr and 2 Y can be distributed. In Fig. 2, panels (d) and (e) show the effect on the total energy as the relaxed separation of the Y atoms in the NNN shell is varied from $a/\sqrt{2}$ to $a\sqrt{5/2}$. The energy differences between the different Zr/Y NNN configurations are only ~ 1 meV/cation so that all are likely to coexist in a material at room temperature. The energy is expressed per cation in the cell because the number of anions per cell varies with Y_2O_3 composition. The range of energies involved can be used as an estimate of the uncertainty in the difference between the $t \rightarrow c$ configurations. The difference between the minimum energies of the 95-atom supercell with the c configuration and that with the t configuration, ΔE^{c-t}, is 0.846 eV. Expressing the latter as an equivalent temperature, this gives 317 ± 15 K/cation, which gives an indication of the relative stability of the YSZ t phase. For the pure ZrO_2 phases, the corresponding calculations give a difference of 534 K/cation, i.e., almost twice as much. It must be noted that the most careful first-principles calculations of the phase transition temperature, obtained in such a way, are not always satisfactory. To get a better quantitative agreement with experiment, the temperature dependence of the vibrational lattice energy must be included in the free energy caculation of each phase.[16]
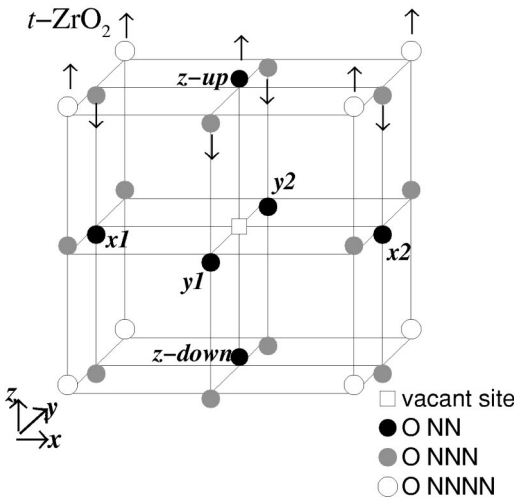
FIG. 3. Ideal positions of O atoms in the t-ZrO$_2$ near the vacancy shown at the fluorite site. The O NN atoms to the □ are labeled.

Each Y atom brings its own local distortion field, which is screened by the NN anions. These relax outwards from the substituted Y atoms by an average distance of 0.1 Å along directions which are close to $\langle 111 \rangle$. This accommodates the longer Y-O bond, which is 2.3 Å in Y$_2$O$_3$ compared to the 1.8 Å of the Zr-O bond in the fluorite structure of pure ZrO$_2$. This result is in agreement with the K-edge XAS findings of Li and co-workers[3] who conclude that the perturbation near to the Y defect is small, indicating that dopant cations do not take an active part in the YSZ stabilization. An isolated □ introduces larger local deformations than the Y defect and these decrease fairly slowly with distance from the □ so that a very large number of atoms are affected. The four sevenfold-coordinated Zr atoms NN to the □ move outward from the □ by 0.18 Å along $\langle 111 \rangle$ directions (in the c cell used), in good agreement with previous calculations.[15]

Figure 3 shows the initial t distortion of the O sublattice. The cubic framework, divided into eight octants, is the same as that in Fig. 1. The unique direction is defined as [001], which is the vertical direction in the figure. Alternate columns of O are displaced up and down by $\delta_{z0} = 0.06a$. The Zr NN atoms are not shown in Fig. 3.

Figure 4 shows the effect of relaxation on the O atoms. The six NN O atoms all move towards the □. The four NN O atoms, close to the equatorial (xy) plane through the origin, all move upward reducing their initial value of δ_z by similar amounts and so remain approximately in an (xy) plane. They also move toward the □ in the xy plane. Note that the lateral shifts are not found in pure t-ZrO$_2$ where only the z displacements occur. The relaxed positions of these four NN O atoms are an average distance of 0.29 Å from the anion sites in fluorite ZrO$_2$. The two apical O NN atoms move in opposite directions along [001]. The upper one in Fig. 4 reduces its initial value of δ_z to close to zero, returning to a position close to that in the c structure. The lower apical NN O atom increases its value of δ_z, becoming the atom with the maximum displacement and also becoming much closer to two of the Zr NN's to the □. The details of the O
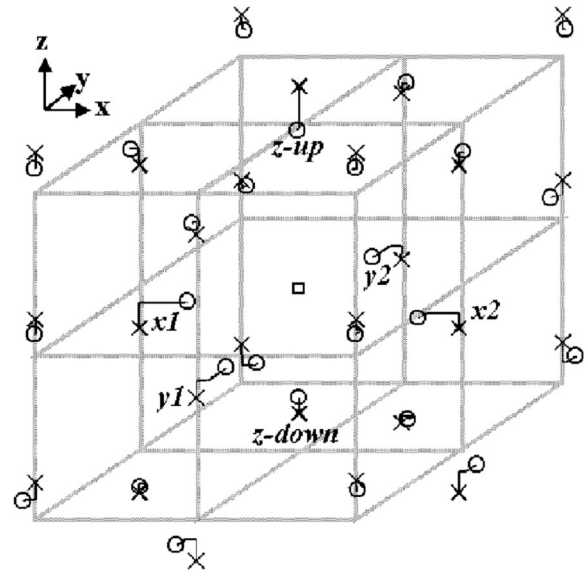

FIG. 4. The effect of relaxation on the O atom positions around the vacancy in t-3.2 mol % YSZ. The vacancy □ is at the center of the figure. The atom positions in the ideal tetragonal structure are shown as $\times$ while the positions in the relaxed structure are shown as $\bigcirc$. The solid lines show the x, y, and z components of the changes in positions. All displacements from the ideal cubic fluorite sites have been doubled for clarity. The two Y atoms in the structure are to the left of the bottom left octant and below the bottom right octant of the diagram.

shifts depend on the positioning of the Y atoms since the Y-O bond length is greater than the Zr-O one. This increases the displacement of O atoms which are NN to Y atoms. Indeed, for the displacements shown in Fig. 4, one Y atom is adjacent to the lower apical NN O while the second Y is bonded to the equatorial O atom, labeled as $x1$ in Fig. 3.

Figure 5 shows how the distances from the □, defined simply as an empty anion site in ideal c-ZrO$_2$, change on relaxation in the c and t cases. In both cases, the NN O atoms end up closer to the □ than the NN Zr atoms. The one
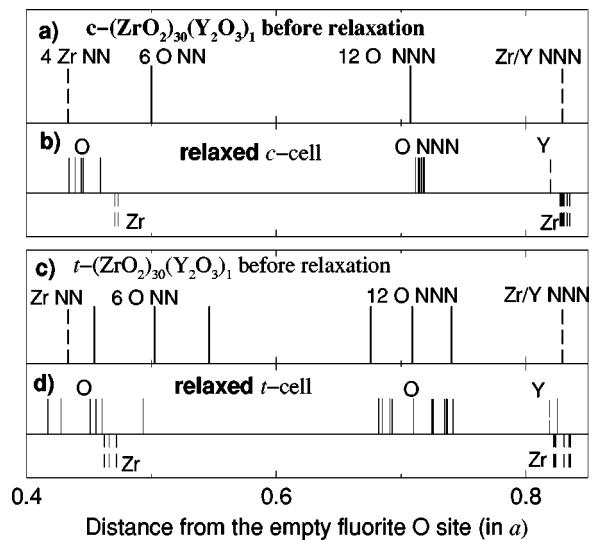

FIG. 5. Distances from the O vacancy for neighboring atoms in the c- and t-3.2 mol % YSZ before and after relaxation.
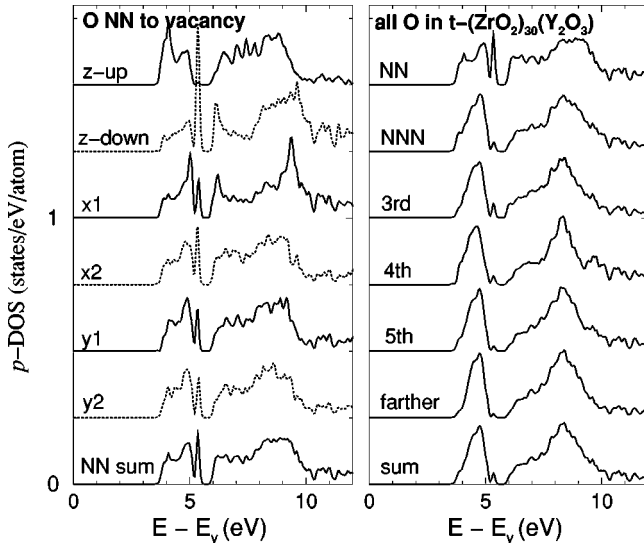
FIG. 6. The p-projected DOS of O in the t-3.2 mol % ZrO_2-Y_2O_3. DOS of each NN site to vacancy are plotted in the left panel while their weighted sum together with the corresponding sums of each anion shell are shown in the right panel.

FIG. 7. Relaxation in the di-□ YSZ, with Y NNN to each vacancy. The energies are plotted vs the □-pair direction in the top panel. The three possible chains of atoms along [111] are shown in the middle panel. In the lower panel, a detailed optimization is shown for each atomic cluster with the □ pair along [111].

exception is in the t-configuration where the upper apical NN O atom is close to the position in the original fluorite structure. The displacements in the (xy) plane decrease with distance from the □. Within the cell, the average displacement in the z direction, δ_z, is only 60% of that in pure t-ZrO_2. Thus, the result of the relaxation is that there are a large number of nonequivalent O sites. However, since the displacements decrease with distance from the □, the environments in each subsequent shell of O atoms around the □ become more similar to that of the perfect structure.

The left panel of Fig. 6 shows the unoccupied p-projected DOS on the six NN O atoms to the □ and their sum. Here the zero of energy is the top of the valence band. The right-hand panel shows the sum of the O p-projected DOS for atoms in successive shells normalized per atom. The fourth and higher anion shells are incomplete because of the limited size of the 95-atom cell, and only those atoms within the cell are summed. It is clear that there are severe modifications to the p-projected DOS in the NN O shell but that these decrease rapidly on moving to atoms in more distant shells. The biggest change occurs in the lower apical O NN, marked "z-down" in Fig. 3. This O is very close to two of the NN Zr atoms because of the effect of both the □ and the adjacent Y atom in the NNN cation shell. The upper apical O NN atom has a p-projected DOS resembling that in the ideal fluorite structure. Three of the O NN atoms in the (xy) plane, namely, $x2$, $y1$, and $y2$, have similar p-projected DOS, while $x1$, which has a Y atom adjacent to it, is significantly different. In the NNN O shell, the four O atoms with adjacent Y atoms also have noticeably different p-projected DOS compared to the eight that only have Zr neighbors. However, these differences are less marked.

Experimentally, EELS finds that the fundamental band gap is 4.2 eV in t-YSZ.[17] After relaxation, the mono-□ model of t-YSZ indicates a gap of 3.7 eV without any midgap states, in good agreement with the experiment. As shown
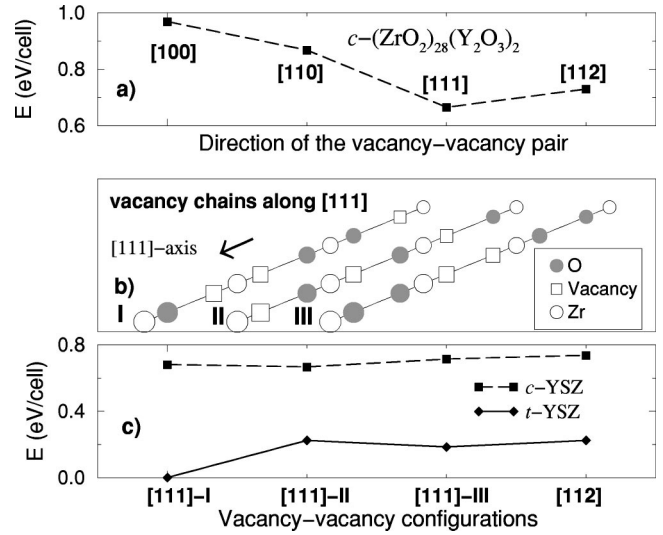
in Fig. 6, the weighted sum of the O p-projected DOS reveals two pronounced peaks above the top of the valence band, E_v, at 4.5 eV and 8 eV, separated by the pseudogap, which can be associated with the e_g-t_{2g} DOS splitting expected in a simple ligand field model of the bonding in ideal c-ZrO_2.

In metal oxides where the pure phase is stable, e.g., SnO_2, CaO, and MgO, thermochemical reduction results in color centers, which can be detected in the optical absorption spectrum[18] and by electron paramagnetic resonance (EPR) measurements.[19] Color centers can also be detected in UV- or x-ray-irradiated zirconia-based samples, in such materials reduced in a low-pressure O atmosphere and in calcia-stabilized zirconia.[20] The presence of the □'s in YSZ might suggest the formation of color centers in this material. DFT calculations neglecting relaxation have been used to predict the presence of color centers,[21] as would our calculations using unrelaxed structures. However, experimentally, 12 and 24 mol % YSZ show no photoactive signal by EPR (Ref. 20) and Y_2O_3 is never used as a coloring agent in YSZ. Thus the color centers are not present in the real material. This is in agreement with our results for the relaxed structures, where the states in the gap present in the unrelaxed cell are no longer present.

B. Divacancy

A 94-atom cell models 6.7 mol % Y_2O_3-ZrO_2. Placing the four Y not closer than NNN shells to each □ and maintaining the maximum number of Y atoms on the NNN shell at 2, several configurations have been relaxed. We investigated vacancies aligned along four directions and the results in the top panel of Fig. 7 show that those along $\langle 111 \rangle$ have the lowest energy. The middle panel shows that there are three possible configurations along $\langle 111 \rangle$ in the 94-atom cell. Electrostatic considerations suggest that □'s should repel.
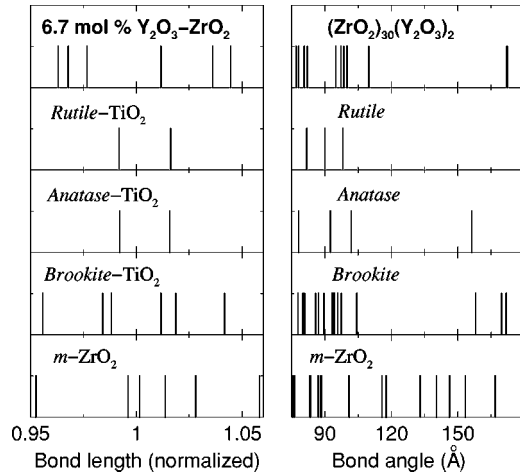
FIG. 8. Bond M-O lengths and M-O-M angles (M=Zr,Ti) in the sixfold-coordinated polyhedra of the relaxed 2□ YSZ cell compared to those observed in the various TiO$_2$ structures as well as in m-ZrO$_2$.

From this point of view, configuration II in the middle panel of Fig. 7 should be energetically favorable as it has the largest separation between □'s and results in sevenfold-coordinated Zr ions. However, the bottom panel in Fig. 7 shows that all three configurations have similar energies in the c case while, in the t case, configuration I has the lowest energy by ∼0.2 eV/cell (80 K/cation). The ⟨112⟩ results are shown to demonstrate that it is a higher-energy configuration in the t case as well as in the c case. In the lowest-energy configuration, the two □'s are along the fluorite [111] direction and are separated by a sixfold-coordinated Zr. The □-cation repulsions acting on the sixfold-coordinated Zr almost compensate each other, resulting in this host ion remaining practically at the original fluorite site. In addition, there are six sevenfold-coordinated NN Zr atoms which relax outwards from the nearest □ in a manner similar to the monovacancy case. This result supports the interpretation of the neutron data by Goff *et al.*[4]

The relaxed cluster of O atoms about the sixfold-coordinated Zr forms a distorted octahedron with Zr-O bond lengths in the range 2.04–2.21 Å. The left panel of Fig. 8 compares the bond lengths, normalized to the mean value for this octahedron, to those in various forms of TiO$_2$ and the polyhedron around sevenfold-coordinated Zr in m-ZrO$_2$. The right panel of Fig. 8 compares the metal-O-metal bond angles in these structures. It is clear that the bond length distributions in the O polyhedron around sixfold-coordinated Zr lie between those around Ti in anatase/rutile and brookite while the bond angle distribution is closest to that in brookite. ZrO$_2$ exibits no regular crystal structure with sixfold co-ordination and density functional theory (DFT) calculations[22] predict the energy of ZrO$_2$ in the rutile structure to be higher than in any of the observed ZrO$_2$ phases. Because of the small size of Zr^{4+}, the electrostatic arguments place ZrO$_2$ on the border between the eightfold-coordinated fluorite and sixfold-coordinated rutile structures.[22] The presence of the larger Y atoms appears to shift this balance in favor of seven-fold and sixfold coordination environments for Zr that are
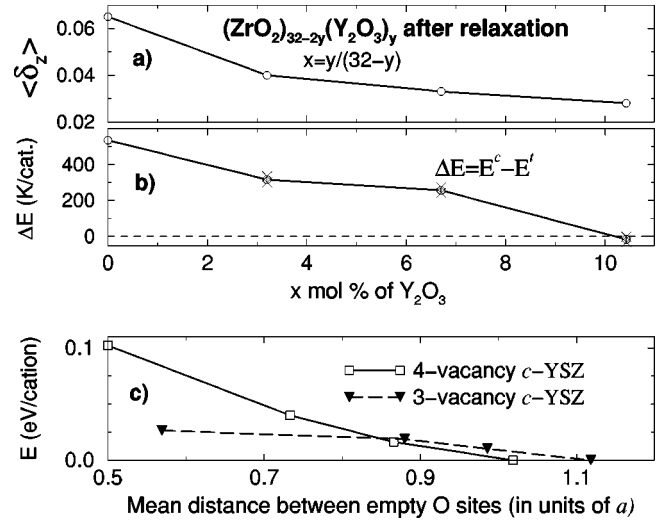

FIG. 9. Two upper panels (a) and (b) illustrate mean t distortion of the O sublattice and the difference in energy between the t and c configurations, respectively. The relaxed energies of the 3□ and 4□ c-YSZ vs mean shortest distance between vacant O sites are shown in the lower panel (c).

similar to the local environments observed in the m-ZrO$_2$ and brookite structures, respectively.

The □ pair along ⟨111⟩ and the sixfold-coordinated NN Zr may play a key role in the stabilization of YSZ. Bogicevic *et al.*[23] have also reported that the sixfold-coordinated Zr appears in the most energetically favorable relaxed compositions of long-range-ordered Zr$_3$Y$_4$O$_{12}$. They note that this shows that the prevailing m-phase driving-force model for YSZ,[24] which assumes that the c-phase stabilization arises from the sevenfold coordination tendency for Zr as in m-ZrO$_2$, may be not absolutely correct. The brookite-type Zr-O motif sometimes can appear in the low-energy configurations of the multivacancy YSZ c cell at higher Y$_2$O$_3$ concentrations discussed below.

C. Multivacancy in YSZ

Unfortunately, the time-consuming lattice algebra technique[25] cannot be utilized to relax all configurations in multi-□ YSZ. Several 3□ and 4□ complexes have been relaxed, allowing investigation of 10.4 and 14.3 mol % Y$_2$O$_3$-ZrO$_2$, respectively. In each configuraton, the Y atoms have been distributed so that they are not closer than NNN to any □. However, this means that the number of Y in the NNN shell can rise to 4. Forcing Y to remain on the NNN sites at 14.3 mol % Y$_2$O$_3$ concentration may not result in the lowest-energy configuration.

In the tri-□ cell, corresponding to 10.4 mol % YSZ, the □'s prefer to be distributed randomly although this means that □'s can end up close together along ⟨111⟩ or ⟨112⟩. However, the di-□ along ⟨111⟩ giving rise to a sixfold co-ordination Zr atom is not energetically favorable in this cell. Panel (a) in Fig. 9 shows that the mean tetragonal distortion ⟨δ$_z$⟩ in the lowest-energy t configuration decreases steadily as the number of □'s increases. Panel (b) in Fig. 9 shows the

difference in energy between the most stable c and t configurations. The energy is given in kelvin per cation to give an indication of the relative stabilities of the c and t phases in terms of thermal energy. In pure ZrO_2 as well as in the monovacancy and divacancy YSZ cells, the t configuration is more stable, while for three $\square$'s, the c configuration is marginally more stable. The changeover in stability is close to that observed experimentally.

The $\square$-$\square$ separation before relaxation can be chosen as a useful parameter in many-vacancy YSZ to categorize its energetics.[23] In the ideal fluorite structure, the position of each vacancy and the distance to any another $\square$ are well defined. The shortest $\square$-$\square$ distance for each empty fluorite site in the cell and, as the result, an average shortest distance between vacancies, $\langle d_{\square\text{-}\square} \rangle$, can be calculated. For example, Fig. 9 shows that the highest-energy configuration calculated has a value of $\langle d_{\square\text{-}\square} \rangle$ equal to $0.5a$. In this configuration, the $\square$'s occupy half (4/8) of the NN anion sites to the same Zr, forming two $\square$-$\square$ pairs along $\langle 100 \rangle$ in different z planes. Each vacancy has another one at a distance $0.5a$, giving an average of $0.5a$. After relaxation, the positions of the vacancies can be changed due to broken symmetry but we believe that the unrelaxed $\langle d_{\square\text{-}\square} \rangle$ is rather a good parameter to illustrate energetics of defect YSZ. In Fig. 9, panel (c) shows the repulsion tendencies between the $\square$'s consistent with both electrostatics and the Zr coordination lowering model. Each total-energy curve in this panel is plotted with respect to its lowest-energy configuration. In the $3\square$ cell, the lowest energy value corresponds to the cell with all vacant O sites separated by $\langle d_{\square\text{-}\square} \rangle = a\sqrt{5}/2$ from each other in a way that creates only sevenfold-coordinated Zr.

D. Soft lattice vibrations

It is known that the main contribution to the structural phase transition comes from particular vibrational modes.[26] The effective phonon potential can be defined in terms of the difference in total energy between the perfect and distorted lattices for various amplitudes of the atomic displacements corresponding to the symmetry of the phonon considered.

In pure ZrO_2, a zone-boundary soft phonon X_2^- which breaks the c symmetry of the O sublattice, displacing the O atoms toward their positions in the t phase, might be responsible for the $c \rightarrow t$ phase tranformation.[14] Our calculation of the X_2^--phonon frequency within the harmonic approximation yields an imaginary frequency of 5.3 THz, which is very close to previous calculations.[14,27] The imaginary frequency simply indicates that the c-ZrO_2 is unstable at low temperatures. If experimental data[28] were available for this mode, then allowance for anharmonicity within a self-consistent phonon approximation [29] would give a quantitative criterion to model the temperature dependence of the phonon frequency as well as the spectrum density. For doped ZrO_2, no microscopic mechanism for the phase transformation initiation has been proposed up to now. We believe that a theoretical investigation of a vibration mode in YSZ which corresponds to the X_2^--phonon of pure c-ZrO_2 will be helpful in understanding the role of of atomic vibrations in the phase transitions of YSZ.
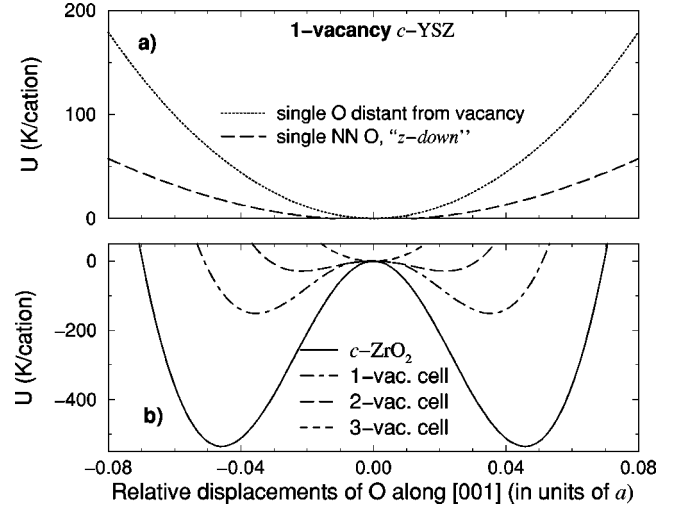

FIG. 10. Single-well and double-well potentials in c-YSZ. The top panel (a) shows the changes in total energy of the $1\square$ YSZ as a single very distant O to vacancy or NN lower O (marked z-down in Fig. 3) are moved from their relaxed positions, demonstrating the soft vibrations of the latter atom. In the panel (b), a decay of the double-well potential in c-YSZ with Y_2O_3 doping shown as U vs the t displacements of O for each concentration of Y_2O_3.

Figure 10 displays the effective potential U, defined as the change in the total energy of the defective YSZ cell as a single O [panel (a)] or all O atoms [panel (b)] are moved from their equilibrium positions by a fixed amount along the z axis. These values of U were calculated using the FEMD method. At the different Y_2O_3 concentrations, the energy curves as functions of the amplitude of the O t displacements, d_z, in units of a, are shown after shifting to a common zero energy at $d_z = 0$. Figure 10(b) illustrates the development of a double-well potential. The U's were normalized per cation, since a number of cations in the cells is unchanged while the numbers of anions change with Y_2O_3 concentration. For 10 mol % Y_2O_3, U has a single minimum at $d_z = 0$. With decreasing Y_2O_3 content, U develops two minima; i.e., its form becomes similar to that of the X_2^- phonon in pure c-ZrO_2. The relative temperature units used give an idea of the temperature required for the $t \rightarrow c$ transition.

A large excess heat capacity ΔC_p has been observed[30] in YSZ at low and room temperatures for 7.8, 9.7, and 11.4 mol % Y_2O_3 compared to the heat capacity calculated from those of pure ZrO_2 and Y_2O_3 by the additivity rule: $\Delta C_p = C_p^{YSZ} - [(1-x)C_p^{ZrO_2} + x C_p^{Y_2O_3}]$. Such an anomaly might be a result of softening in lattice vibrations. ΔC_p decreases with increasing the dopant concentration,[30] suggesting that the softening mode vanishes gradually with increasing Y_2O_3 content. The lower panel of Fig. 10 shows that this effect comes mainly from the soft X_2^- phonon. However, in 11.4 mol % Y_2O_3, where the calculation shows that this soft phonon has vanished, δC_p is nonzero. This suggests the possibility of another kind of softening in lattice vibrations.

The upper panel of Fig. 10 shows U in the mono-$\square$ YSZ c cell when an individual O atom is displaced while all other anions are fixed at their relaxed positions. Two O were dis-
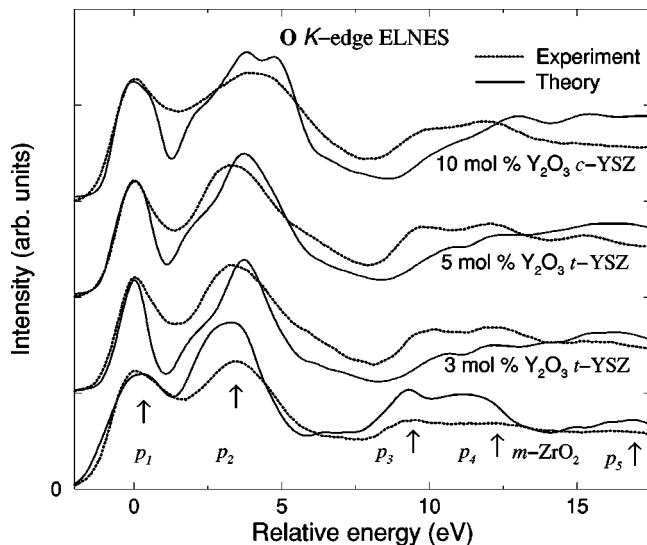
FIG. 11. Experimental O K-edge ELNES for the m-ZrO_2, t- (3 and 5 mol % Y_2O_3-ZrO_2), and 10 mol % c-Y_2O_3-ZrO_2) compared with corresponding calculations for m-ZrO_2 and defective YSZ.

placed in the mono-□ c cell to illustrate the effect of (i) the lower apical NN O to the □ along [001] and (ii) an O outside the fifth anion shell to □. This may indicate a marked softening of the vibration mode for the O NN atoms with respect to the distant ones. Hence, there is a possible mechanism of softening in the c phase of YSZ which can give a small excess heat capacity. Certainly, the NN O atoms have higher amplitudes of vibrations and this may have an effect on the ELNES shape.

E. ELNES

The calculated ELNES is shown in Fig. 11 and compared to the experimental O K-edge data for m-ZrO_2 and for YSZ with Y_2O_3 contents in the range 3–10 mol %. The energy of the first peak p_1 has been defined as zero, and the experimental and calculated shapes have been aligned and intensity matched at this energy. In the calculations, the weighted sum of O K-edge ELNES for all types of O sites has been made, taking into account the theoretical core-level shifts. Taking m-ZrO_2 first, there is good agreement between the calculated and experimental O K-edge shapes with peak positions up to 10 eV. Beyond that, the calculation becomes less reliable. Using the model of YSZ with relaxed defects, the agreement

between experiment and theory for the depth and shape of the minimum between the first two low-energy peaks p_1 and p_2 has been improved significantly compared to that using pure ZrO_2 structures.[7] We have reported elsewhere[6] that the energy separation between peaks p_1 and p_2 in the experimental O K-edge ELNES is essentially linearly dependent on dopant concentration. This behavior appears to be independent of the crystalline phase of the material and is reflected in the calculations. The energy separation between the p_1 and p_2 may prove to be a useful parameter for the characterization of zirconia ceramics on a nanometer scale. As described in Sec. II, great care was taken to minimize the effects of electron beam damage on the results discussed in this paper. In the case of high-spatial-resolution analysis it is possible that the high current density will result in the creation of metal and oxygen vacancies through electron beam damage processes and care is required to ensure that the observed ELNES is not influenced by such processes.

V. CONCLUSIONS

In summary, we report that features of the experimental O K-edge ELNES shapes depend on the crystal structures and the Y_2O_3 composition and provide us with further information to improve our understanding of YSZ. *Ab initio* calculations were performed to obtain the O K-edge ELNES in the relaxed YSZ. Good agreement between calculated and measured ELNES data was obtained with respect to the number of maxima, the intensity ratios, and energy positions of the peaks. In studying YSZ we have demonstrated that the relaxation of defects plays an important role. Our calculations relate the detailed changes in the relaxed structure to the experimentally observed ELNES shapes and their variation with Y_2O_3 content. Some residual differences between experiment and the calculated ELNES are likely to result from the soft-mode vibrations because, in EELS, there will be no essential difference for the static atomic displacements from the dynamical case of thermal vibrations. The combination of ELNES with detailed theoretical modeling shows great potential for the characterization of doped metal oxides.

*Present address: Department of Physics, University of Warwick, Coventry CV4 7AL, United Kingdom.

†Present address: Department of Physics, University of Ioannina, 45110 Ioannina, Greece.

[1] E. C. Subbarao, in *Science and Technology of Zirconia*, edited by A. H. Heuer and L. W. Hobbs, *Advances in Ceramics*, Vol. 3 (American Ceramic Society, Metals Park, OH, 1981).

[2] M. H. Tuilier, J. Dexpert-Ghys, H. Dexpert, and P. Lagarde, J. Solid State Chem. **69**, 153 (1987).

[3] P. Li, W. Chen, and J. E. Penner-Hahn, Phys. Rev. B **48**, 10 063 (1993); **48**, 10 082 (1993).

[4] J. P. Goff, W. Hayes, S. Hull, M. T. Hitchings, and K. N. Clausen, Phys. Rev. B **59**, 14 202 (1999).

[5] H. G. Scott, Acta Crystallogr., Sect. B: Struct. Crystallogr. Cryst. Chem. **33**, 281 (1977).

[6] D. Vlachos, A. J. Craven, and D. W. McComb, J. Phys.: Condens. Matter **13**, 10 799 (2001).

[7] S. Ostanin, A. J. Craven, D. W. McComb, D. Vlachos, A. Alavi, M. W. Finnis, and A. T. Paxton, Phys. Rev. B **62**, 14 728 (2000).

[8] A. J. Craven, J. Microsc. **180**, 250 (1995).

[9] A. Alavi, J. Kohanoff, M. Parrinello, and D. Frenkel, Phys. Rev. Lett. **73**, 2599 (1994).

[10] M. Methfessel and M. van Schilfgaarde, *NFP Manual 1.01* (IHP, Frankfurt/Oder, 1997).

[11] A. T. Paxton, M. van Schilfgaarde, M. MacKenzie, and A. J. Craven, J. Phys.: Condens. Matter **12**, 729 (2000).

[12] D. A. Muller, J. Singh, and J. Silcox, Phys. Rev. B **57**, 8181 (1998).

[13] O. Keski-Rahonen and M. O. Krause, At. Data Nucl. Data Tables **14**, 139 (1974).

[14] S. Fabris, A. T. Paxton, and M. W. Finnis, Phys. Rev. B **63**, 094101 (2001).

[15] G. Stapper, M. Bernasconi, N. Nicoloso, and M. Parrinello, Phys. Rev. B **59**, 797 (1999).

[16] S. Ostanin and V. Trubitsin, Phys. Rev. B **57**, 13 485 (1998).

[17] D. W. McComb, Phys. Rev. B **54**, 7094 (1996).

[18] Y. Chen, V. M. Orera, R. Gonzalez, R. T. Williams, G. P. Williams, G. H. Rosenblatt, and G. J. Pogatshnik, Phys. Rev. B **42**, 1410 (1990).

[19] V. M. Orera, R. I. Merino, Y. Chen, R. Cases, and P. J. Alonso, Phys. Rev. B **42**, 9782 (1990); R. Ben-Michael, D. S. Tannhauser, and J. Genossar, *ibid.* **43**, 7395 (1991); C. B. Azzoni and A. Paleari, *ibid.* **44**, 6858 (1991).

[20] C. B. Azzoni and A. Paleari, Phys. Rev. B **53**, 5 (1996).

[21] S. E. Kulkova and O. N. Muryzhnikova, Physica B **192**, 284 (1993); G. A. Ol'khovic, I. I. Naumov, and O. I. Velikokhatnyi, J. Phys.: Condens. Matter **7**, 1273 (1995).

[22] M. W. Finnis, A. T. Paxton, M. Methfessel, and M. van Schilfgaarde, Phys. Rev. Lett. **81**, 5149 (1998).

[23] A. Bogicevic, C. Wolverton, G. M. Crosbie, and E. B. Stechel, Phys. Rev. B **64**, 014106 (2001).

[24] E. V. Stefanovich, A. L. Shluger, and C. R. A. Catlow, Phys. Rev. B **49**, 11 560 (1994).

[25] L. G. Ferreira, S.-H. Wei, and A. Zunger, Int. J. Supercomput. Appl. **5**, 34 (1991).

[26] A. D. Bruce and R. A. Cowley, *Structural Phase Transitions* (Taylor & Francis, London, 1984).

[27] F. Detraux, P. Ghosez, and X. Gonze, Phys. Rev. Lett. **81**, 3297 (1998).

[28] D. W. Liu, C. H. Perry, A. A. Feinberg, and R. Currat, Phys. Rev. B **36**, 9212 (1987); D. N. Argyriou and M. M. Elcombe, J. Phys. Chem. Solids **57**, 343 (1996).

[29] S. Ostanin, E. Salamatov, and V. Trubitsin, Phys. Rev. B **57**, 5002 (1998).

[30] T. Tojo, T. Atake, T. Mori, and H. Yamamura, J.Therm. Anal. Calor. **57**, 447 (1999).